ABSTRACT

Title of dissertation: Measuring topology of BECs
in a synthetic dimensions lattice

Dina Genkina
Doctor of Philosophy, 2018

Dissertation directed by: Professor Ian Spielman
Department of Physics

Measuring topology of BECs in a synthetic dimensions lattice

by

Dina Genkina

Dissertation submitted to the Faculty of the Graduate School of the
University of Maryland, College Park in partial fulfillment
of the requirements for the degree of
Doctor of Philosophy
2018

Advisory Committee:
Professor Ian Spielman, Chair/Advisor

Table of Contents

List of Tables

List of Figures

Chapter 3: Atom Light Interactions

3.1 Atomic structure

Alkali atoms (those in the first column of the periodic table) are the most amenable to laser cooling because their energy level structure is relatively simple. It can be understood as primarily the energy state of the single electron in the outer shell, interacting with the rest of the atom—the nucleus and all the other electrons—as a whole. The quantum numbers that describe the energy levels of the atom are the radial quantum number of the outermost electron N, that electron's spin S, the orbital angular momentum L, and finally the nuclear spin I. The work described in this thesis was done with alkali species ^{87}Rb and ^{40}K.

3.1.1 Fine and hyperfine sturcutre

The spin orbit interaction, or coupling between L and S, give rise to the fine structure of the atom. This is the splitting of energies according to the quantum number J, where the operator $\mathbf{J} = \mathbf{L} + \mathbf{S}$ and $|L-S| \leq J \leq |L+S|$. The ground state of ^{87}Rb, in term notation $N^{2S+1}L_J$ is $5^2S_{1/2}$, where S is orbital notation indicating $L = 0$. Since $L = 0$, the ground state only has one possible value of $J = 1/2$, and there is no ground state hyperfine splitting. The first excited state 5^2P_J has orbital angular momentum $L = 1$ (as indicated by P in orbital notation. Therefore, J can take on two different values: 1/2 and 3/2, producing a hyperfine splitting between the $5^2P_{1/2}$ and $5^2P_{3/2}$. The energy splitting between the ground $5^2S_{1/2}$ and lower

excited $5^2P_{1/2}$ level is conventionally called the $D1$ line, and the splitting between $5^2S_{1/2}$ and $5^2P_{3/2}$ is the $D2$ line. For other alkalis, including ^{40}K, the ground state structure is identical and only the N value is different. Therefore, even though their energies vary, $D1$ and $D2$ lines feature in all alkalis.

There is also a contribution from the nuclear spin $\mathbf{I}$, which gives rise to hyperfine structure of the states. For ^{87}Rb, $I = 3/2$ and for ^{40}K, $I = 4$. The total spin, including nuclear spin, is indicated by the quantum number F, and $|J - I| \leq F \leq |J + I|$. The interaction with the nuclear spin splits the ground state of ^{87}Rb into two manifolds, $F = 1$ and $F = 2$. Similarly for ^{40}K, it splits the ground state into $F = 9/2$ and $F = 7/2$ manifolds. The structure of the ground and first excited states of ^{87}Rb and ^{40}K, including both the fine and hyperfine splittings, is diagrammed in Figure ??. Note that the $D1$ and $D2$ transitions are in the optical regime, making them amenable to laser cooling. The fine structure splitting of the excited states is in the far infrared, whereas the hyperfine splitting of the ground states is in the microwave regime.

3.1.2 Interaction with static magnetic fields

In a static background magnetic field $\mathbf{B}$, the atomic angular momentum interacts with the field via the Hamiltonian

$$H_B = \frac{\mu_B}{\hbar}(g_S \mathbf{S} + g_L \mathbf{L} + g_I \mathbf{I}) \cdot \mathbf{B}, \tag{3.1}$$

where μ_B is the Bohr magneton, g_S, g_L and g_I are the spin, orbital and nuclear Lande g-factors correcting their respective magnetic dipole moments. Without loss of generality, we can define the magnetic field to be in the $e_{\mathbf{z}}$ direction, $\mathbf{B} = B_z e_{\mathbf{z}}$, to obtain

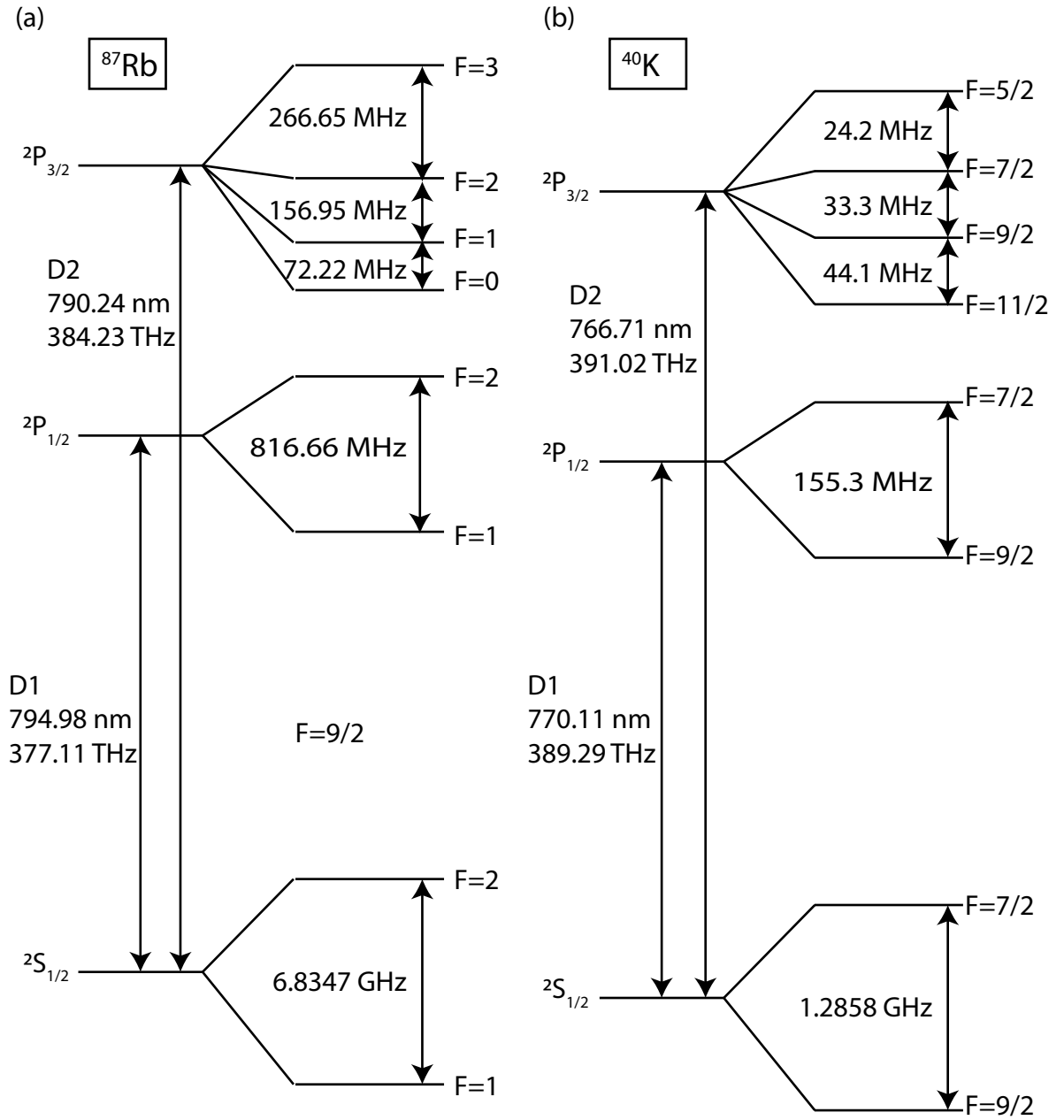$$H_B = \frac{\mu_B}{\hbar}(g_S S_z + g_L L_z + g_I I_z) B_z. \tag{3.2}$$

Figure 1: Atomic structure of the ground and first excites states, with fine and hyperfine splittings. (a)^{87}Rb. Values from [?]. (b). ^{40}K. Values from [?].

At very low magntic field strengths, where the energy shift due to H_B is small compared to the hyperfine splitting, the total angular momentum F remains a good quantum number, and the Hamiltonian in eqn. **??** can be re-written as

$$H_B = \frac{\mu_B}{\hbar}(g_F F_z)B_z, \tag{3.3}$$

where the effective Lande g-factor is dependent on the angular momentum quantum numbers:

$$g_F = g_J \frac{F(F+1) - I(I+1) + J(J+1)}{2F(F+1)} + g_I \frac{F(F+1) + I(I+1) - J(J+1)}{2F(F+1)}. \tag{3.4}$$

In this regime, the levels split linearly according to the F_z projection quantum number, m_F. For the ground state of ^{87}Rb, it splits into three hyperfine states in the $F = 1$ manifold ($m_F = 0, \pm 1$) and five hyperfine states in the $F = 2$ manifold ($m_F = 0, \pm 1, \pm 2$). This regime is at fields $B \leq \approx 1$ Gauss for ^{87}Rb, as seen in Figure **??**.

At fields producing energy shifts small compared to the fine structure splitting, but not negligible compared to the hyperfine splitting, F is no longer a good quantum number, and the relevant Hamiltonian becomes

$$H_B = \frac{\mu_B}{\hbar}(g_J J_z + g_I I_z)B_z. \tag{3.5}$$

Here, since $g_I \ll g_J$, the energy dependence on B_z is dominated by a linear dependence on the J_z projection quantum number, m_J, as seen in the higher field limit in Figure **??**.

In the intermediate regime, there is in general no analytic solution for the eigenenrgies and one must resort to numerics. However, for the specific case of $J = 1/2$ applicable to alkali ground states, there is an analytic solution given by the
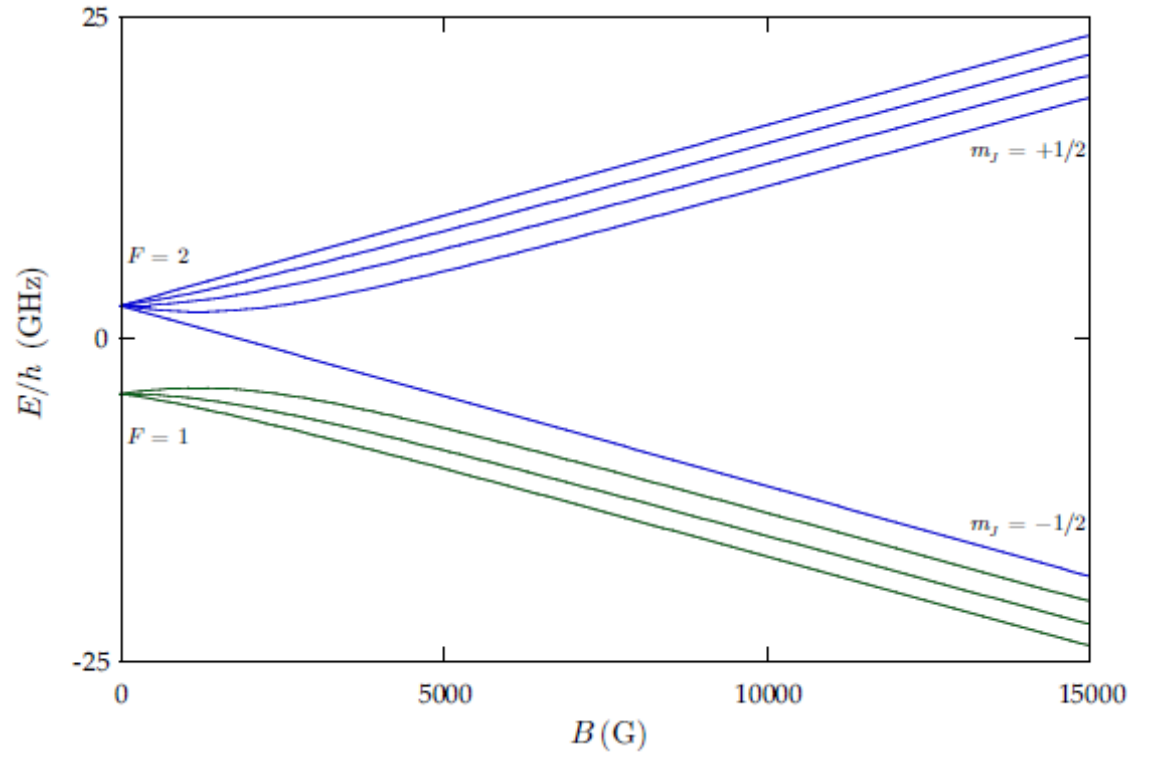
Figure 2: Energy structure of hyperfine states of the ground state of ^{87}Rb as a function of external magnetic field strength in Gauss. Figure from ref. [?]

Breit-Rabi formula [?]:

$$E_{|J=1/2 m_J I m_I\rangle} = -\frac{\Delta E_{hfs}}{2(2I+1)} + g_I \mu_B m B \pm \frac{\Delta E_{hfs}}{2} \left(1 + \frac{4mx}{2I+1} + x^2 \right)^{1/2}, \quad (3.6)$$

where ΔE_{hfs} is the zero field hyperfine splitting, $m = m_I \pm m_J$, and

$$x = \frac{(g_J - g_I)\mu_B B}{\Delta E_{hfs}}. \quad (3.7)$$

From this we can get a better picture of the shifts at low fields, where $\mu_B B \ll E_{hfs}$. Expanding eqn. ?? to second order in small parameter $4mx/(2I+1) + x^2$, and neglecting the field-independent terms, we obtain

$$\Delta E_{|J=1/2 m_J I m_I\rangle} \approx \frac{\Delta E_{hfs}}{2} \left(\frac{1}{2} \left[\frac{4mx}{2I+1} + x^2 \right] - \frac{1}{8} \left[\frac{16m^2 x^2}{(2I+1)^2} + \frac{4mx^3}{2I+1} + x^4 \right] \right). \quad (3.8)$$

We recognize the term linear in mx, $E_{hfs} mx/(2I+1) = (g_J - g_I)\mu_B B m/(2I+1)$. In addition, there is a term quadratic in mx:

$$\Delta E_{hfs} \frac{m^2 x^2}{(2I+1)^2} = \frac{(g_J - g_I)^2 \mu_B^2 B^2 m^2}{\Delta E_{hfs}(2I+1)^2} = \epsilon(B)m^2, \quad (3.9)$$

where in the last term we have defined $\epsilon(B)$, the magnitude of this 'quadratic' Zeeman energy shift. For the magnetic field strengths used in experiments described in this thesis, the linear term plus quadratic correction are sufficient for describing the energy levels.

The form of the approximate Hamiltonian in this regime for any value of F is given by

$$H_0 = H_{\mathrm{KE}} + \hbar \omega_z \mathbf{F_z} + \hbar \epsilon \mathbf{F_z}^2, \quad (3.10)$$

where $\hbar \omega_z = \mu_B g_F B_z / \hbar$, and the kinetic energy Hamiltonian $H_{\mathrm{KE}} = \hbar^2 \vec{k}^2 / 2m\mathcal{I}$, and $\mathcal{I}$ is the identity matrix.

3.2   Near-resonant atom-light interaction

In this section, we will assume the atom can be treated as a two-level system: one with a ground and excited atomic state, with an energy difference of energy difference $\hbar\omega_0$. When such an atom, starting in the ground state, is illuminated by a laser beam with frequency $\hbar\omega_{\rm L}$, there are three kinds of transitions that occur: during aborption the atom aborbs a photon from the laser and goes from the ground to the excited state; during stimulated emission, the atom emits a photon into the field of the laser beam and jump from the excited to the ground state; during spontaneous emission, the atom decays to the ground state from the excited state with no help from the laser, emitting into a random vacuum mode. Stimulated emission results in coherent light co-propagating with the laser beam, while spontaneous emission results in light scattering incoherently in any direction. The rate of spontaneous emission from an excited state is given by the natural transition linewidth of the atomic transition Γ.

3.2.1   Rabi oscillations

On timescales short compared to $1/\Gamma$, spontaneous emission can be ignored, and an atom undergoes coherent Rabi oscillations between the ground and excited states via cycles of absorption and stimulated emission [?]. Let us consider the Hamiltonian

$$H = H_0 + H_{\rm L}(t), \tag{3.11}$$

where H_0 is the bare atomic Hamiltonian and $H_{\rm L}$ is the interaction with the laser beam. We can write the wavefunction Ψ as a linear combination of the two eignestates (for a two-level atom) of the bare Hamiltonian as

$$\Psi = c_g(t)\phi_g(\mathbf{r})e^{-i\omega_g t} + c_e(t)\phi_e(\mathbf{r})e^{-i\omega_e t}, \tag{3.12}$$

where $c_g(t)$ and $c_e(t)$ are the time-dependent coefficients multiplying the eigenstate wavefuntions ϕ_g and ϕ_e of the ground and excited state respectively, and $\mathbf{r}$ is the spatial cooridnate. Absorbing any diagonal elements of H_{L} into H_0, multiplying both sides of the Schroedinger equation from the left by ψ_j and integrating over $\mathbf{r}$, we can write down the Schroedinger equation as two coupled equations:

$$i\hbar\frac{dc_g(t)}{dt} = c_e(t)H_{\mathrm{L}}^{ge}(t)e^{-i\omega_0 t} \tag{3.13}$$

and

$$i\hbar\frac{dc_e(t)}{dt} = c_g(t)H_{\mathrm{L}}^{eg}(t)e^{i\omega_0 t}, \tag{3.14}$$

where $H_{\mathrm{L}}^{ge}(t)$ is the off-diagonal element of the laser coupling Hamiltonian that couples the excited to the ground state and $H_{\mathrm{L}}^{ge}(t) = H_{\mathrm{L}}^{eg*}(t)$. This coupling Hamiltonian can be written in terms of the electric field produced by the laser beam coupling to the electric dipole moment of the atom as

$$H_{\mathrm{L}}^{ge}(t) = \hbar\Omega\cos(kz - \omega_{\mathrm{L}}t) \tag{3.15}$$

with

$$\Omega = \frac{-eE}{\hbar}\int \phi_g(\mathbf{r})\mathbf{r}\phi_e(\mathbf{r})dr \tag{3.16}$$

the Rabi frequency, characterizing the coupling strength between the laser field (with amplitude E) and the atom. Here, e is the charge of the electron. The Rabi frequency can also be related to the natural linewidth of the atomic transition Γ via $\Omega^2 = \frac{\Gamma\lambda_L^3}{h(2\pi)^3}I$, with λ_L as the laser wavelength, h as Plank's constant and I as the laser intensity.

To solve this Schroedinger equation, we make the traditional transformation

to the rotating frame:

$$c'_g(t) = c_g(t) \tag{3.17}$$

$$c'_e(t) = c_e(t)e^{-i\delta t}, \tag{3.18}$$

where $\delta = \omega_0 - \omega_L$ is the detuning of laser light from resonance. In this frame, we can write the atom-light Hamiltonian in the $\begin{pmatrix} c'_g \\ c'_e \end{pmatrix}$ basis as:

$$H = \hbar \begin{pmatrix} -\delta/2 & \Omega/2 \\ \Omega/2 & \delta/2 \end{pmatrix}. \tag{3.19}$$

In the limit of no coupling, $\Omega = 0$, in the rotating frame the eigenenegies are $E_{\pm} = \pm\hbar\delta/2$. For non-zero coupling, finding the eigenvalues of H gives

$$E_{\pm} = \pm\hbar\sqrt{\delta^2 + \Omega^2}/2. \tag{3.20}$$

The eigenenrgies are shifted in the presence of the light.

Assuming the atom starts in the ground state $c_g(t = 0) = 1$, we can solve the Shroedinger equation with the above Hamiltonian

$$i\hbar\frac{d}{dt}\begin{pmatrix} c'_g \\ c'_e \end{pmatrix} = H\begin{pmatrix} c'_g \\ c'_e \end{pmatrix} \tag{3.21}$$

we obtain the oscillating excited state population

$$c'_e(t) = -i\frac{\Omega}{\sqrt{\Omega^2 + \delta^2}}\sin\left(\frac{\sqrt{\Omega^2 + \delta^2}t}{2}\right), \tag{3.22}$$

known as Rabi oscillations. The frequency of these oscillations is the generalized

Rabi frequency $\Omega' = \sqrt{\Omega^2 + \delta^2}$. The amplitude of the oscillation is maximum when the laser is on-resonance, $\delta = 0$. As the detuning increases, the contrast in excited and ground populations decreases, while the frequency of the oscillation increases.

3.2.2 Scattering

In the regime where spontaneous emission cannot be ignored, Rabi oscillations of each individual atom are intermittently interrupted by decay to the ground state. Averaging over an atomic ensamble, on the time scale of a single Rabi oscillation the overall excited state population reaches a steady state, and the rate of spontaneous emission becomes constant. Since during spontaneous emission the ejected photon can go into any vacuum mode, this process can be thought of as the scattering of photons by the atoms. This scattering rate is given by [?]

$$\gamma_{\mathrm{sc}} = \frac{\Gamma}{2} \frac{I/I_{\mathrm{sat}}}{1 + 4(\delta/\Gamma)^2 + I/I_{\mathrm{sat}}}, \tag{3.23}$$

where I_{sat} is the saturation intensity. This is the intensity at which the timescale of spontaneous emission matches the Rabi oscillation rate, reducing the capacity for absorption of extra light.

3.2.3 Adiabatic rapid passage

3.3 Far-off resonant atom-light interaction

We can infer the behavior of atoms in a far-detuned laser field by taking the near resonant solutions from eqns. ?? and ?? in the limit $\delta \gg \Omega$. First, looking at the excited state population in eqn. ??, the amplitude of the excited state population oscillation approaches zero. Therefore, as expected, no absorption of the light actually takes place and the atom remains in the ground state. However, the
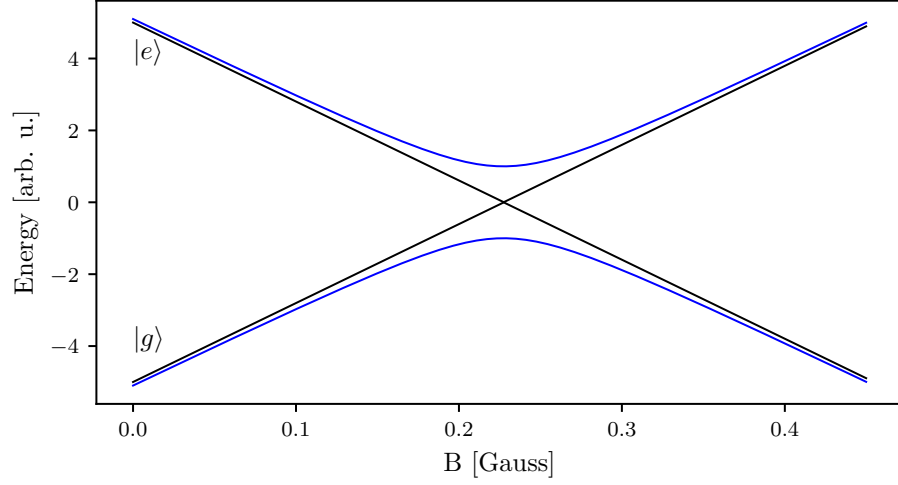
Figure 3:

light still effects the atom by shifting the eigenenergies via eqn. **??**. Recalling that the bare eigenenrgies in the rotating frame are given by $E_\pm = \pm\hbar\delta/2$, the energy shift from bare is given by

$$\Delta E_\pm = \pm\hbar\sqrt{\delta^2 + \Omega^2}/2 - \pm\hbar\delta/2 \tag{3.24}$$

Expanding the energy shift in the small parameter Ω/δ, we obtain the shifted energies $E_\pm = \pm\hbar\sqrt{\delta^2 + \Omega^2}/2 \approx \pm(\delta/2 + \Omega^2/4\delta)$. The shift from bare energy levels is thus

$$\Delta E_\pm \approx \pm\hbar(\delta/2 + \Omega^2/4\delta) - \pm\hbar\delta/2 = \pm\hbar\Omega^2/4\delta. \tag{3.25}$$

This laser intensity dependent energy shift is called the AC Stark shift, and is the basis of most laser created potentials for cold atoms.

For the ground state, and a red detuned laser beam (where the laser frequency is lower than the resonant frequency), this creates energy minima in locations of maximal laser intensity. For the lattice described in this chapter, as well as for the trapping of our atoms in the final stages of cooling, we use high power (up to 10 W)

lasers with wavelength $\lambda_L = 1064$ nm.

3.4   Absorption imaging

Absorption imaging takes advantage of the on-resonant interaction described in the previous section. An on or near-resonant laser beam ($\delta/\Gamma \ll 1$) is shined at the atoms, and the aborbed light acts to create a shadow in the shape of the atoms in the laser beam. This beam with the shadow is then imaged on a camera, in our case a CCD, as depicted in Figure ??a (top). This is called the atom image, and the intensity distribution over the camera is denoted by $I_f(x, y)$, where the subscript f stands for final - the intensity after the light has encountered the atoms. To quantify the 'shadowed out' intensity, after the atoms have left the trap the same laser intensity is shined directly at the camera, as in Figure ??a (bottom). This is called the probe image, and the intensity distribution over the camera is denoted by $I_0(x, y)$, where the subscript 0 indicated initial - the intensity before the light had encountered the atoms.

To recover the atom number distribution encountered by the light, consider an atomic cloud with 3D density $\rho(x, y, z)$. Since we can only obtain 2D information from the camera, we can only hope to recover a 2D atomic column density $n(x, y) = \int \rho(x, y, z) \mathrm{d}z$. Focusing in on a single pixel of the camera, we can consider a single value of I_0 and I_f to recover a local n. As the laser light propagates through the atomic cloud, the intensity of the light will diminish due to absorption. This absorption as a function of propagation direction z can be expressed using the scattering rate equation Eq. ?? as the number of photons scattered by the atoms (proportional to the atomic density times the scattering rate) times the photon energy $\hbar\omega_{\mathrm{L}}$:

$$\frac{d}{dz}\frac{I(z)}{I_{\mathrm{sat}}} = -\hbar\omega_{\mathrm{L}}\rho(z)\gamma_{sc}(z) = -\rho(z)\sigma_0\frac{I(z)/I_{\mathrm{sat}}}{1 + 4\delta^2/\Gamma^2 + I(z)/I_{\mathrm{sat}}}, \tag{3.26}$$
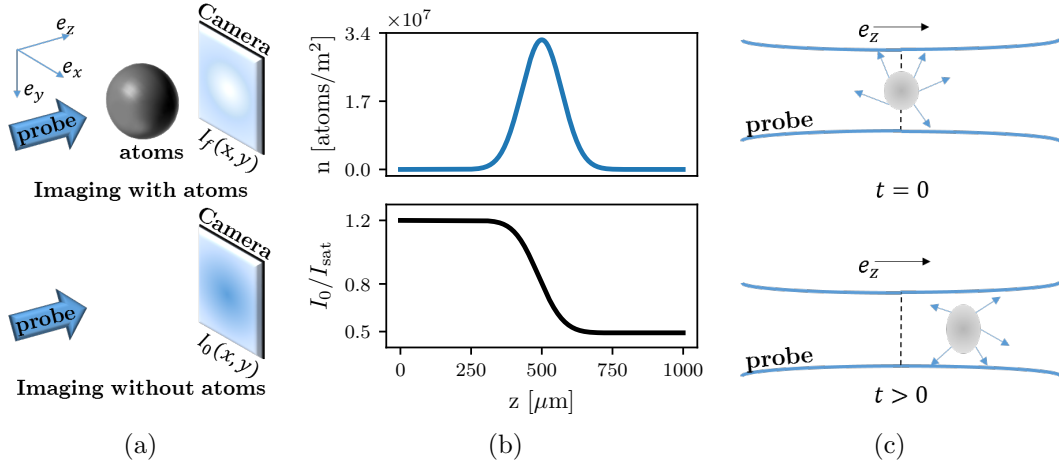
Figure 4: Absorption imaging. (a) Near resonant probe light illuminates the atoms, and the transmitted light (containing a shadow of the atoms) is imaged on the camera. A second image taken with no atoms provides a reference. (b) The probe beam is partially absorbed as it traverses the cloud, and the intensity seen by atoms further along the imaging direction $e_{\mathbf{z}}$ is lowered. (c) An atomic cloud illuminated by a probe light field absorbs photons from the probe and re-emits them in all directions. This process results in a net acceleration of the cloud in the direction of the probe light as well as diffusive spreading in the transverse directions.

where the resonant scattering cross section is $\sigma_0 = 3\lambda_0^2/2\pi$, and λ_0 is the wavelength asociatted with atomic resonance.

Integrating both sides of Eq. **??**, we obtain

$$\sigma_0 n = \left(1 + 4\delta^2/\Gamma^2\right)\ln(I_0/I_f) + (I_0 - I_f)/I_{\text{sat}}. \tag{3.27}$$

The quantity $OD = ln(I_0/I_f)$ is called the optical depth of the cloud. When the probe intensity I_0 is much smaller than the saturation intensity, the second term in Eq. **??** becomes negligible. Assuming further that the probe light is on resonance, $\delta = 0$, the atomic column density becomes simply $\sigma_0 n = OD$. Figure **??**b shows a Gaussian atomic density distribution (top) and the resulting probe intensity as a function of position in the cloud (bottom). The intensity drops from its initial to final value gradually as it traverses the cloud.

However, there is an important effect that the above equations do not account for. Namely, as the atoms absorb light from the probe beam, they also get a momentum kick equal to the momentum of a photon during each collision $\hbar k_r = h/\lambda_L$ in the direction of propagation. It is true that the absorbed photon will then be re-emitted by the atom, inducing a loss of momentum, but since this happens through the process of spontaneous emission into a random vacuum mode, the average momentum kick acquired this way over many re-emissions will average to zero. On average, each photon absorbed will induce a change in velocity of the atom of $v_r = \hbar k_r/m$, where m is the atomic mass, as depicted in Fig. **??**c. As the velocity of the atom changes, due to the Doppler effect, the apparent laser frequency will change as well. Therefore, even if the laser light is exactly on-resonant for a stationary atom, it will become off-resonant for longer imaging times, and Eq. **??** will acquire a time dependence. For most experiments, this effect is small and can be neglected. However, if the imaging time becomes of order a recoil time t_r, a time after which the recoil-induced detuning δ becomes of order Γ, this effect becomes significant. We explore this effect in Chapter **??**.

3.4.1 Time-of-flight and in situ imaing

There are two commonly used protocols for measuring cold atomic clouds, in situ and time of flight measurements. Generally, the atomic cloud is trapped (in our case by an optical dipole trap) during the experiment. In situ is Latin for in its original place. As suggested by the name, in situ measurements are taken while the cloud is still in its original trap, or immediatly after the trap is turned off before any dynamics have had time to occur. These measurments measure the real spatial distribution of the atoms at the end of the given experiment. There is a difficulty asscoiated with making in situ measurments of BECs, however. Namely, BECs in their original trap tend to be relatively dense, with optical depths often in excess of

$OD \approx 20$, requiring unrealistic probe light intensities to resolve. One way to bypass this difficulty is to selectively image only a small fraction of the condensed atoms, as was done with microwave imaging for our magnetic field stabilization feedforward protocol [INSERT SECTION REFERENCE HERE ONCE ITS WRITTEN]. Another option is to instead perform a time-of-flight measurement.

In time-of-flight measurements, the trapping potential is abruptly snapped off after the experiment, and the atoms are allowed to free fall and expand for some time t. For our experiments, t was on the order of tens of miliseconds. In the regime where time t is long enough that the atoms travel much further than the initial extent of the cloud in the directions transverse to the imaging axis, the final position of the atoms is determined almost exclusively by their in situ momentum, not their in situ position. Therefore, time-of-flight imaging in this regime measures the atomic distribution as a function of momentum, not position.

3.5   One dimensional optical lattices

3.5.1   Lattice Hamiltonian

Our 1-D optical lattice is created by retro-reflecting the $\lambda_L = 1064$ nm laser, creating a standing wave of light. Via the AC Stark shift, this creates a periodic potential for the atoms of the form

$$V = V_0 \sin^2(k_L x), \tag{3.28}$$

where $k_L = 2\pi/\lambda_L$ is the wavenumber associated with the lattice recoil momentum. The time-independent Hamiltonian, for some eigenenergy E_n, will be given by

$$-\frac{\hbar^2}{2m}\frac{d^2}{dx^2}\Psi_n(x) + V_0 \sin^2(k_L x)\Psi_n(x) = E_n\Psi_n(x). \tag{3.29}$$

Since the potential is spatially periodic, we can invoke Bloch's theorem [?]:

$$\Psi_{n,q} = e^{iqx}u_{n,q}(x), \tag{3.30}$$

where q is the crystal momentum restricted to $\pm\hbar k_L$, and $u_{n,q}(x)$ is the spatially varying part of the wavefunction. Plugging this in to the Hamiltonian, we obtain

$$-\frac{\hbar^2}{2m}\left(-q^2 + 2iq\frac{d}{dx} + \frac{d^2}{dx^2}\right)u_{n,q}(x) + V_0\sin^2(k_L x)u_{n,q}(x) = E_n u_{n,q}(x). \tag{3.31}$$

Expanding $u_{n,q}(x)$ in Fourier components commensurate with the lattice period of $2k_L$ as $u_{n,q}(x) = \sum_{j=-\inf}^{\inf} a_j e^{i2k_L jx}$, we obtain

$$\sum_j \left(\frac{\hbar^2}{2m}(q + 2k_L)^2 a_j + V_0\sin^2(k_L x)a_j\right)e^{i2k_L jx} = E_n \sum_j a_j e^{i2k_L jx}. \tag{3.32}$$

Re-writing $\sin^2(k_L x) = (e^{-2ik_L x} + e^{2ik_L x} - 2)/4$, multiplying both sides by $e^{i2k_L j'x}$ and invoking $\sum c_j e^{ik(j-j')} = \delta_{jj'}$, where $\delta_{jj'}$ is the Kroniker delta and c_j are appropriately normalized coefficients, we get for any value of the index j

$$\frac{\hbar^2}{2m}(q + 2k_L j)^2 a_j - \frac{V_0}{4}(a_{j+1} + a_{j-1}) = E_n a_j. \tag{3.33}$$

This can be expressed in matrix form

$$
H_L = \begin{pmatrix}
\ddots \\
& \frac{\hbar^2}{2m}(q+4k_L)^2 & \frac{V_0}{4} & 0 & 0 & 0 \\
& \frac{V_0}{4} & \frac{\hbar^2}{2m}(q+2k_L)^2 & \frac{V_0}{4} & 0 & 0 \\
& 0 & \frac{V_0}{4} & \frac{\hbar^2}{2m}q^2 & \frac{V_0}{4} & 0 \\
& 0 & 0 & \frac{V_0}{4} & \frac{\hbar^2}{2m}(q-2k_L)^2 & \frac{V_0}{4} \\
& 0 & 0 & 0 & \frac{V_0}{4} & \frac{\hbar^2}{2m}(q-4k_L)^2 \\
& & & & & & \ddots
\end{pmatrix},
$$

(3.34)

in the basis of momentum orders $|k\rangle = e^{ikx}$ given by:

$$
\begin{pmatrix}
\vdots \\
|q+4k_L\rangle \\
|q+2k_L\rangle \\
|q\rangle \\
|q-2k_L\rangle \\
|q-4k_L\rangle \\
\vdots
\end{pmatrix}.
$$

(3.35)

This matrix can be diagonalized for every value of the crystal momentum q, with the resulting band structure shown in Figure ??. It is convenient to define the lattice recoil energy $E_L = \hbar^2 k_L^2 / 2m$. Then, we can re-write the Hamiltonian with
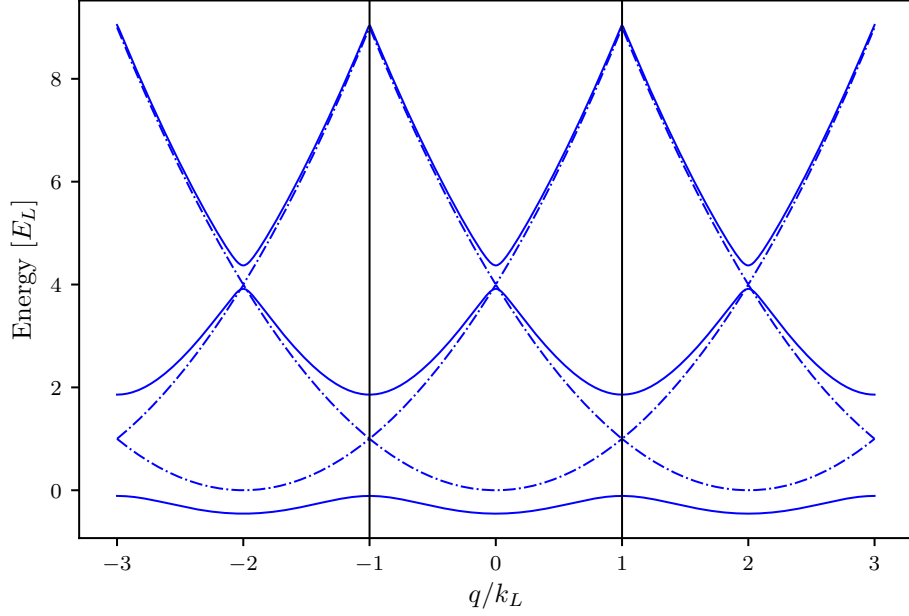
Figure 5: Lattice band structure in the extended zone scheme. The dashed lines represent the limit of zero lattice depth, with the regular parabolic dispersion relation of a free particle repating with reciprocal lattice period. The solid lines are the dispersion relation at $V_0 = 4.0E_L$, showing the opening of gaps at crossings of the zero lattice depth bands. The black lines demarcate the first Brillouin zone.

V_0 in units of E_L and momenta q in units of k_L as

$$H_L/E_L = \begin{pmatrix} \ddots & & & & & \\ & (q+4)^2 & \frac{V_0}{4} & 0 & 0 & 0 \\ & \frac{V_0}{4} & (q+2)^2 & \frac{V_0}{4} & 0 & 0 \\ & 0 & \frac{V_0}{4} & q^2 & \frac{V_0}{4} & 0 \\ & 0 & 0 & \frac{V_0}{4} & (q-2)^2 & \frac{V_0}{4} \\ & 0 & 0 & 0 & \frac{V_0}{4} & (q-4)^2 \\ & & & & & \ddots \end{pmatrix}. \qquad (3.36)$$

In any numerical simulation, the number of momentum orders that can be included is finite. We determine the value of the parameter $n = \max(|j|)$ as the

lowest n at which the eigenvalues stop changing to machine precision from $n-1$. The code for finding and plotting the eigenvalues and eigenvectors of the lattice hamiltonian is included in Appendix [MAKE APPENDIX WITH CODE?].

3.5.2 Tight binding approximation

In the limit of large lattice depths, $V_0 >\approx 5E_L$, the lattice Hamiltonian is well approximated by the tight-binding model. In the tight binding model, the basis is assumed to be a set of orthogonal functions, called Wannier functions, localized to each lattice site $|j\rangle$. The approximation lies in assuming only nearest neighbor tunnelings between the sites, forming the tight-binding Hamiltonian

$$H_{\text{tb}} = -t\,|j\rangle\,\langle j+1| + \text{H.c.}, \tag{3.37}$$

where t is the tunneling amplitude between nearest neighbor sites and H.c. stands for Hermitian conjugate. We have neglected the diagonal kinetic energy term, as it will be equal for every Wannier function $|j\rangle$ and thus represents a constant energy offset. All the information about the lattice depth is therefore reflected in the tunneling amplitude t.

The tight binding Hamiltonian can also be expressed in the momentum basis by Fourier transforming the basis functions:

$$|j\rangle = \frac{1}{\sqrt{N}} \sum_{k_j} e^{-ik_j j}\,|k_j\rangle\,, \tag{3.38}$$

giving the Hamiltonian

$$H_{\text{tb}} = -\frac{1}{N} \sum_{k_1} \sum k_2 t\, e^{-ijk_1} e^{ik_2(j+1)}\,|k_1\rangle\,\langle k_2| + \text{H.c} = 2t\cos(k)\,|k\rangle\,\langle k|\,. \tag{3.39}$$

From this we can directly read off the band structure of the tight binding Hamilto-

nian. First, we notice that we only obtain one band - to approximate higher bands with the tight binding approximation we would need to construct a different set of Wannier functions and a different tunneling strength. Second, we see that the lowest band is simply a cosine - therefore we have solved for the band structure without even defining what the basis Wannier functions are! Third, the amplitude of the cosine function is given by the tunneling strength t. This gives us a good clue as to how to determine the appropriate tunneling given a lattice depth V_0 - simply find a t that matches the amplitude of the lowest band, which becomes cosinusoidal in the deep lattice limit.

The precise form of the Wannier functions depends on both the depth of the lattice and the band being reproduced. It is not necessary for us to find their full expression, as the band structure can be calculated without them. The definition, however, is

$$|j\rangle = \int_{\mathrm{BZ}} e^{i\phi(q)-iqja}\Psi_q(x)\mathrm{d}q, \tag{3.40}$$

where the integral is over the Brillouin zone, from $-k_L$ to k_L, a is the lattice spacing $\lambda_L/2$, and Ψ_q is the Bloch wavefunction at crystal momentum q, and $\phi(q)$ is the phase associated with each Bloch wavefuntion. The Bloch wavefunctions individually have arbitrary phase. The phase plays an important role in combining the Bloch wavefunctions into a Wannier function, finding the proper phase relationship to make the wavefunction maximally localized at each site [**?**].

3.5.3 Pulsing vs adiabatic loading of the lattice

The lattice depth parameter $V_0/4$, for a range of values, can be well calibrated experimentally by pulsing on the lattice. Here, the word pulsing indicates that the lattice is turned on fully non-adiabatically, if not instantaneously, such that the original bare momentum state is projected onto the lattice eigenbasis, as shown in

Figure **??**a. If the atoms start out stationary in the trap, the bare state in the momentum basis is simply

$$|\Psi_0\rangle = \begin{pmatrix} \vdots \\ 0 \\ 0 \\ 1 \\ 0 \\ 0 \\ \vdots \end{pmatrix}, \qquad (3.41)$$

as depicted in Figure **??**b.

Since the lattice eigenbasis is distinct from the bare one, instiantaneously turning on the lattice will necessarily excite the atoms into a superposition of lattice eigenstates, each evolving with a different phase according to the eigenenergy while the lattice is on, as shown in Figure **??**c. Then, when the lattice is snapped back off, the wavefunction is projected back into the bare basis, and the varying phase accumulation results in a beating of the different momentum orders, see Figure **??**d. This can be calculated simply by using the time evolution operator

$$|\Psi(t)\rangle = e^{-iH_L t/\hbar} |\Psi_0\rangle . \qquad (3.42)$$

By pulsing on the lattice for variable amounts of time t, we can obtain fractional populations in the different momentum states. Time-of-flight imaging captures the momentum distribution of the cloud, and the different entries of $\Psi(t)$ in the momentum basis will thus appear as different clouds on the absorption image, as shown in Figure **??**a. The fractional population in these clouds corresponds to a measurement of $|a_j|^2$. Typically for our values of the lattice depth $V_0 < 10E_L$, it is sufficient to simply count three central momentum orders, $k = q, q \pm 2k_L$. Then, we can fit Eq.
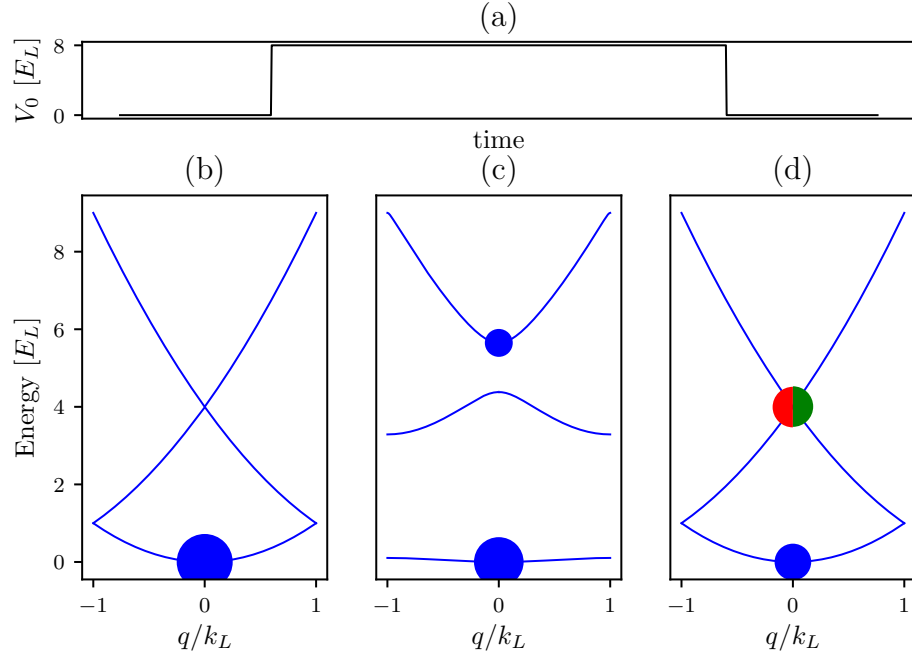
Figure 6: Lattice pulsing. (a) Lattice depth as a function of time during a pulsing experiment. The lattice is turned on instantaneously at $t = 0$ and held on for a variable amount of time until being turned off instantaneously at a final time $t = t_f$. (b) Atomic population before $t = 0$. The dispersion relation is that of a free particle, and all of the atoms start out at $q = 0$ in the lowest energy level. Here, the area of the dots is proportional to the fractional population in the energy state. (c) Atomic population after the lattice is turned on for a lattice depth of $V_0 = 8.0E_L$. The energy spectrum now shows the lattice band structure, and some atomic population is projected onto the excited bands. (d) Atomic population after the lattice is snapped off at $t_f = 150~\mu$s. The wavefunction is projected back onto the bare states, with some fraction (blue circle) in the lowest band at $k = 0$ and some fraction in the excited band, with equal population being projected onto the $k = 2k_L$ (green) and $k = -2k_L$ (red).
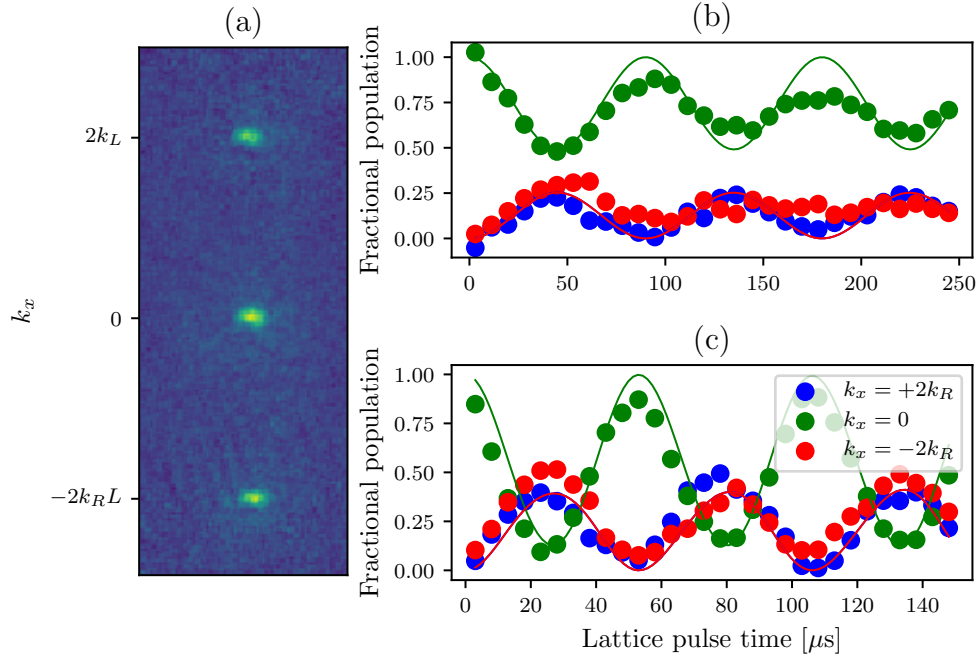
Figure 7: Lattice pulsing for calibration. (a) An example time-of-flight image from a pulsing experiment. The three different clouds are different momentum orders. (b) Fractional populations in the different momentum orders as a function of pulsing time at a low lattice power. Data is indicated by dots and best fit theory is represented by lines. The lattice depth from fit is $V_0 = 5.57 \pm 0.07 E_L$. (c)Fractional populations in the different momentum orders as a function of pulsing time at a higher lattice power. Data is indicated by dots and best fit theory is represented by lines. The lattice depth from fit is $V_0 = 12.69 \pm 0.07 E_L$.

?? to the data with fitting parameter V_0, thus deducing the lattuce depth. Some examples of these pulsing experiments are presented in figure ??b,c.

In contrast to pulsing, adiabatic loading turns the lattice on slowly, such that the atomic wavefunction starting in the bare ground state can continuously adjust to remain in the ground state of the current Hamiltonian, without projecting onto any of the higher bands. This process is illustrated in Figure ??. The adiabatic timescale depends on the spacing between the ground and next excited band (or if starting in a different eigenstate, the nearest eigenstate). If the energy difference between the ground and first excited state is ΔE, the timescale on which the lattice

is turned on must fulfill $t \gg h/\Delta E$.

3.6   Raman and rf coupling

3.6.1   Rf coupling Hamiltonian

For the $F = 1$ manifold, there are three available spin states $m_F = 0, \pm 1$. There are many ways of introducing coupling terms between the different hyperfine states. Here, we will explain two methods: rf coupling and Raman coupling. Rf coupling is a radio-frequency oscillating magnetic field, in our case produced by a pair of circular coils in series side by side above the atoms (see [?]). Assuming the rf oscillating field is polarized along the $\mathbf{e}_x$, with the bias field along $\mathbf{e}_z$, the coupling Hamiltonian is given by $H_{rf} = \mu_B g_F \vec{\mathbf{F}} \cdot \vec{B} = \mu_B g_F \mathbf{F}_x B_x \cos(\omega t)$, where $2\pi\omega$ is the rf frequency. The schematic of this setup is shown in Figure ??. The eignestates of the bare Hamiltonian H_0 are the constituent m_F states. The eigenstates of the coupled Hamiltonian $H_0 + H_{rf}(t)$ can be expressed as a linear superposition of the bare eignestates $\Psi(\vec{x}, t) = \sum_{m_F} c_{m_F}(t) \phi_{m_F}(\vec{x}) e^{-i\omega_{m_F} t}$. The Hamiltonian in this basis can then be written as [?]

$$H_{\text{rf}} = H_{\text{KE}} + \hbar \begin{pmatrix} 0 & \Omega\cos(\omega t)e^{i\omega_z t} & 0 \\ \Omega\cos(\omega t)e^{-i\omega_z t} & 0 & \Omega\cos(\omega t)e^{i\omega_z t} \\ 0 & \Omega\cos(\omega t)e^{-i\omega_z t} & 0 \end{pmatrix}, \qquad (3.43)$$

where Ω is the Rabi frequency, proportional to B_x. We can then transfer into the rotating frame $c'_{m_F} = e^{-im_F \delta t} c_{m_F}$, where $\delta = \omega_z - \omega$. Then we apply the rotating wave approximation, that the fast oscillating terms average to zero over time scales of interest $e^{2i\omega t} \approx 0$, and obtain
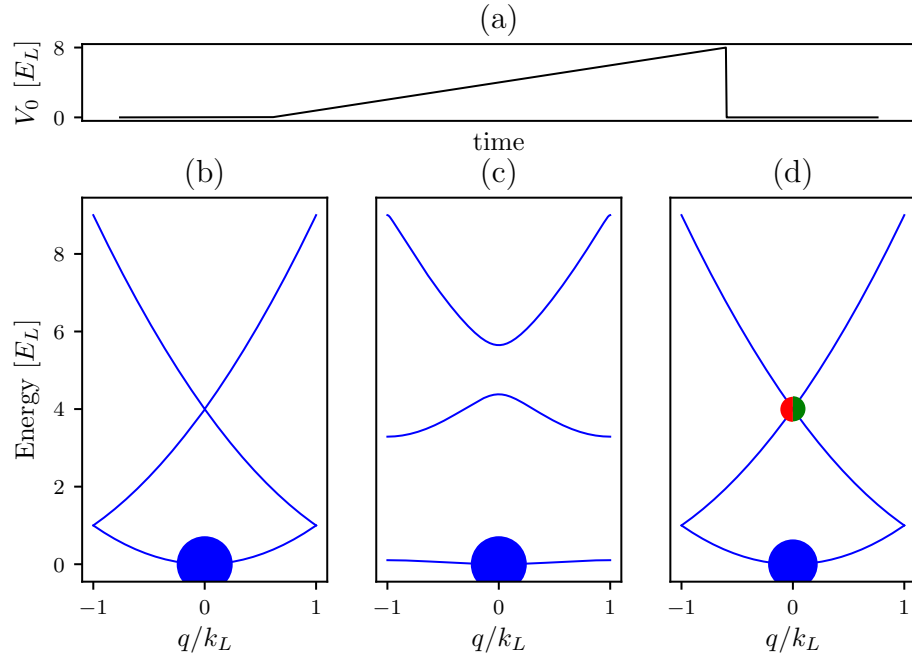
Figure 8: Adiabatic lattice loading. (a) Lattice depth as a function of time during adiabatic turn-on. The lattice is ramped on starting at $t = 0$, slowly increasng to a final lattice depth and turned off instantaneously at a final time $t = t_f$. (b) Atomic population before $t = 0$. All atoms are at $k = 0$ in the lowest bare band. (c) Atomic population after the lattice is turned on adiabatically to a lattice depth of $V_0 = 8.0 E_L$. All atoms remain in the lowest band, but the band is no longer bare. (d) Atomic population after the lattice is snapped off. The wavefunction is projected back onto the bare states, with some fraction (blue circle) in the lowest band at $k = 0$ and some fraction in the excited band, with equal population being projected onto the $k = 2k_L$ (green) and $k = -2k_L$ (red). Since the lowest lattice band is a superposition of bare bands, some atoms are excited to the higher bare bands.
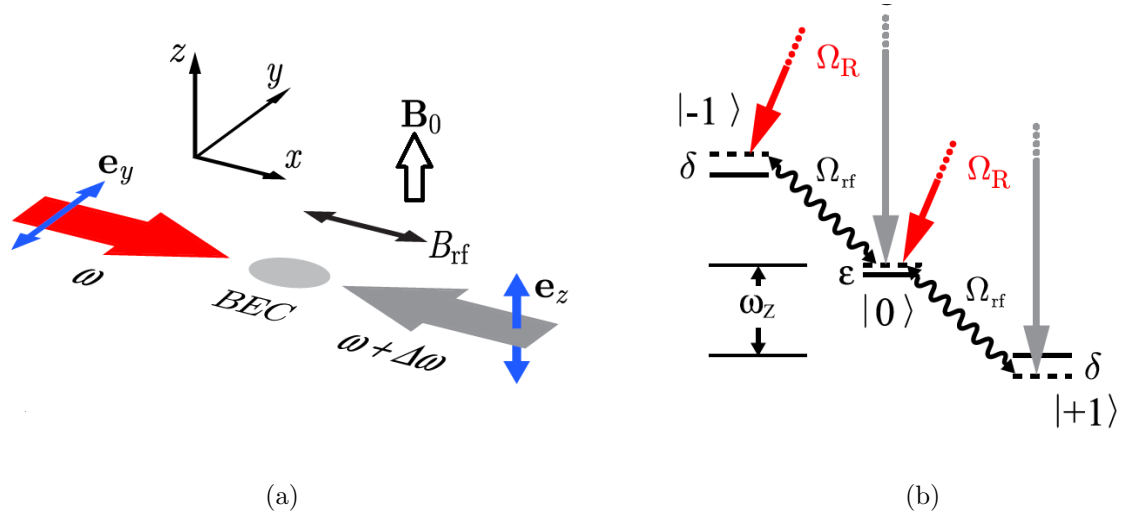
(a)   (b)

Figure 9: Raman and rf coupling schematic. (a) Beam geometry of the Raman beams and rf relative to the external field. The Raman beams have a frequency difference $\Delta\omega$, and are linearly polarized in perpendicular directions. (b) Level structure of both Raman and Rf coupling for hyperfine states of the $F = 1$ manifold. The hyperfine splitting sparates the levels by an energy $\hbar\omega_z$. The quadratic Zeeman shift ϵ lowers the energy of the $m_F = 0$ state, and the detuning δ of either the Raman or the rf fields shifts the energies of the $m_F = \pm 1$ states. Raman transitions are two-photon, exciting up to a virtual state and coming back down to an adjacent hyperfine state, with an accompanying momentum transfer. Rf couples adjacent hyperfine states directly. Figure taken from ref. [?]

$$H_{\mathrm{rf}} = H_{\mathrm{KE}} + \hbar \begin{pmatrix} \delta & \Omega/2 & 0 \\ \Omega/2 & -\epsilon & \Omega/2 \\ 0 & \Omega/2 & -\delta \end{pmatrix}, \tag{3.44}$$

or for any value of F

$$H_{\mathrm{rf}} = H_{\mathrm{KE}} + \hbar\delta F_z + \hbar\epsilon F_z^2 + \Omega F_x/2. \tag{3.45}$$

The band structure of this Hamiltonian can be seen in Figure ??, where we have diaganolized Eq. ?? for a range of momenta k_x (we have islolated k_x for comparison with Raman coupling, as will be seen in the next section). The parabolas are simply the free particle dispersion relations along one dimension, with three

bands arising from the three available spin states. It is convenient to define the magnetization of an eigenstate $m = \sum_{m_F} m_F * p_{m_F}$, where p_{m_F} is the fractional population in the m_F state. We have indicated the magnetization of the eigentate by coloring the eigenenrgies, with $m = -1$ in red, $m = 0$ in green, and $m = +1$ in blue. In Figure ??a, both the detuning and the coupling strength are zero. Therefore, there are simply three free particle dispersions, each exactly correlated with a particular spin state, the $m_F = \pm 1$ are degenerate and the $m_F = 0$ state is slightly offset by the quadratic shift $\hbar\epsilon$. In Figure ??c, the coupling strength is again zero, but the detuning has been turned on, lifting the degeneracy between the $m_F = \pm 1$ states. Figure ??b,d shows the same conditions as a,c, respectively, but with the coupling strength turned on. In Figure ??b, where the detuning is zero and the quadratic shift is negligible compared to the coupling strength, all states average to a magnetization of zero–the $m_F = \pm 1$ states are symmetrically populated. In Figure ??d, this symmetry is broken by the presence of a detuning.

3.6.2 Raman coupling Hamiltonian

The counter-propagating Raman beams, as seen in Figure ??, couple the same states as the rf. The do so via the vector light shift created by the pair of beams. The electric field due to the right going beam (red in Figure ??a) is $\mathbf{E} = E_0\exp(ik_Rx - i\omega t)\mathbf{e}_y$, where E_0 is the amplitude of the electric field and $\hbar k_R = h/\lambda_R = \hbar\omega/c$. The electric field from the left going beam (gray in Figure ??b) is $\mathbf{E} = E_0\exp(-ik_Rx - i(\omega + \Delta\omega)t)\mathbf{e}_z$. This combines to give an effective field from the vector light shift [?] $B_{\text{eff}} \propto \mathbf{E} \times \mathbf{E}^* \propto -E_0^2\cos(2k_Rx + \Delta\omega t)\mathbf{e}_x$. Going through the same procedure as for the rf coupling case, including the transfer into the rotating frame and the rotating wave approximation, we obtain the same Hamiltonian in the basis of bare spin states $|-1\rangle, |0\rangle, |1\rangle$ but with an extra phase factor:
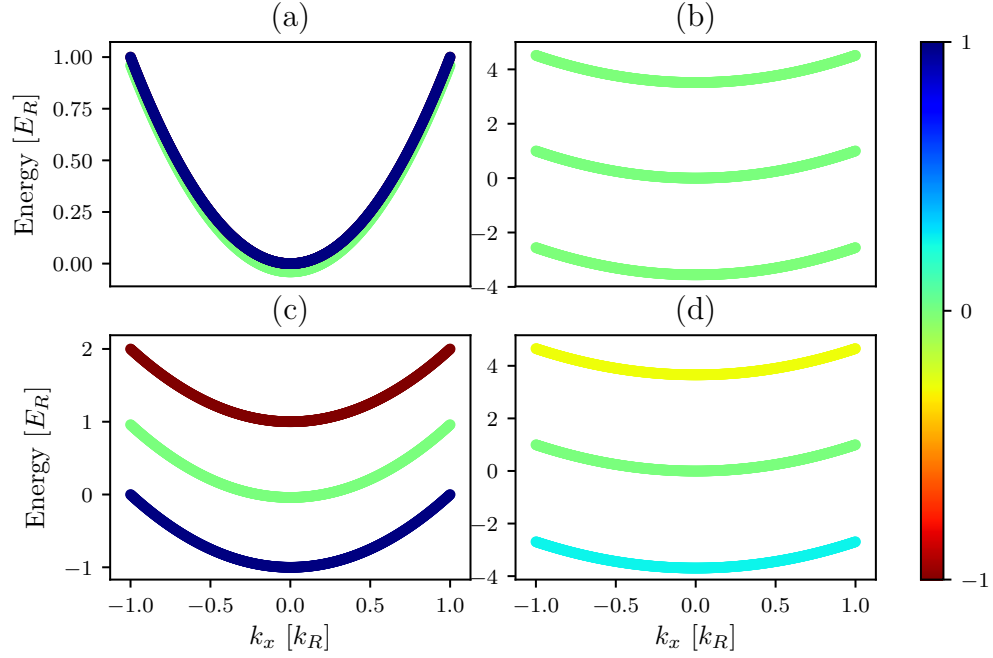
Figure 10: Band structure of the rf Hamiltonian, Eq. **??**, in momentum space. For all plots, the quadratic Zeeman shift $\hbar\epsilon = 0.04E_R$, and the color represents magnetization, labeled by the colorbar. (a) $\hbar\Omega = 0$, $\hbar\delta = 0$. No coupling or detuning is present, so the only separation between the bands is due to the quadratic shift $\hbar\epsilon$. (b) $\hbar\Omega = 5.0E_R$, $\hbar\delta = 0$. (c) $\hbar\Omega = 0$, $\hbar\delta = 1.0E_R$. Even though the coupling strength is zero, the bands are separated by the detuning. (d) $\hbar\Omega = 5.0E_R$, $\hbar\delta = 1.0E_R$.

$$H_{\text{Raman}} = H_{\text{KE}} + \hbar \begin{pmatrix} \delta & \Omega/2e^{-i2k_Rx} & 0 \\ \Omega/2e^{i2k_Rx} & -\epsilon & \Omega/2e^{-i2k_Rx} \\ 0 & \Omega/2e^{i2k_Rx} & -\delta \end{pmatrix}, \qquad (3.46)$$

where $\delta = \omega_z - \Delta\omega$.

This phase difference between the rf and Raman Hamiltonian has an intuitive physical explanation. In order to undergo a Raman transition, an atom first absorbs a photon from one beam, getting a momentum kick equal to the recoil momentum $\hbar k_R$. Then, to decay back down to an adjacent spin state, the undergoes stimulated emission into the field of the other (counter-propagating) beam, acquiring another recoil momentum kick in the same direction for a total of $2\hbar k_R \mathbf{e}_x$. Therefore, the Raman coupling Hamiltonian for $F = 1$, after transforming into the rotating frame and performing the rotating wave approximation, can be written in the same way as the rf Hamiltonian in Eq. **??** with the addition of a momentum kick—in real space, an aquired phase—of e^{i2k_Rx}.

We can again make a basis transformation to get rid of this phase. Let us define $|-1\rangle' = \exp(-2ik_Rx)|-1\rangle = |k_x - 2k_R, -1\rangle$, $|0\rangle' = |0\rangle = |k_x, 0\rangle$, $|1\rangle' = \exp(2ik_Rx)|1\rangle = |k_x + 2k_R, 1\rangle$, where for third definition we went into the momentum basis and labelled the states by a combination of their momentum and spin state. Then, including the kinetic energy term along $\mathbf{e}_x$ explicitly, we obtain the Hamiltonian in the new basis as:

$$H_{\text{Raman}} = H_{\text{KE}}^{(y,z)} + \begin{pmatrix} \frac{\hbar^2(k_x-2k_R)^2}{2m} + \hbar\delta & \hbar\Omega/2 & 0 \\ \hbar\Omega/2 & \frac{\hbar^2 k_x^2}{2m} - \hbar\epsilon & \hbar\Omega/2 \\ 0 & \hbar\Omega/2 & \frac{\hbar^2(k_x+2k_R)^2}{2m} - \hbar\delta \end{pmatrix}. \qquad (3.47)$$

It is convenient to define the Raman recoil energy as $E_R = \frac{\hbar^2 k_R^2}{2m}$. The band structure of this Hamiltonian is shown in Figure **??**, for several representative pa-

rameter values, with the magnetization labelled by the color. Figure **??**a shows the band structure in the limit of zero coupling and zero detuning, but where we have already gone into the basis $|k_x - 2k_R, -1\rangle, |k_x, 0\rangle, |k_x + 2k_R, 1\rangle$; therefore, the free particle parabola corresponding to the $m_F = 1$ spin states is shifted to center on $k_x = -2k_R$ and the $m_F = -1$ parabola is shifted to center on $k_x = 2k_R$. As the coupling is turned on to $\hbar\Omega = 1E_R$ in Figure **??**b, the points where the parabolas cross become 'avoided crossings', separating into three bands where magnetization (and the underlying spin distribution) depends on the momentum k_x. As the coupling strength is turned up even further to $\hbar\Omega = 5E_R$ in Figure **??**c, the lowest band goes from having three minima, one corresponding to each original spin state, to only one minimum. This transition happens at $\hbar\Omega = 4E_R$ [**?**]. In Figure **??**d, we show the band structure again in the limit of zero coupling, but this time with a detuning of $\hbar\delta = 1.0E_R$. Note that the detuning tips the parabolas with respect to each other. Figure **??**e shows the detuned system with coupling strenth turned up to $\hbar\Omega = 1E_R$, still in the three minima regime but with avoided crossings creating three momentum and spin coupled bands. In Figure **??**f, the detuned system is turned up to a coupling strength of $\hbar\Omega = 5E_R$, creating a single minimum, this time offset from $k_x = 0$.

We can write the general F version of the Raman coupled Hamiltonian in the basis $|k_x + m_F * 2k_R, m_F\rangle$, where $-F \leq m_F \leq F$, as:

$$H_{\text{Raman}} = H_{\text{KE}}^{(y,z)} + \hbar^2(k_x\mathcal{I} + 2k_R F_z)^2/2m + \hbar\delta F_z + \hbar\epsilon F_z^2 + \Omega F_x/2. \qquad (3.48)$$

3.6.3   Calibration of Raman and Rf dressed states

To calibrate the rf and Raman coupling strengths, we take a similar approach to the 1-D lattice calibration: start in a pure spin state, for example $m_F = 0$, and turn the coupling on non-adiabatically to induce Rabi oscillations between the
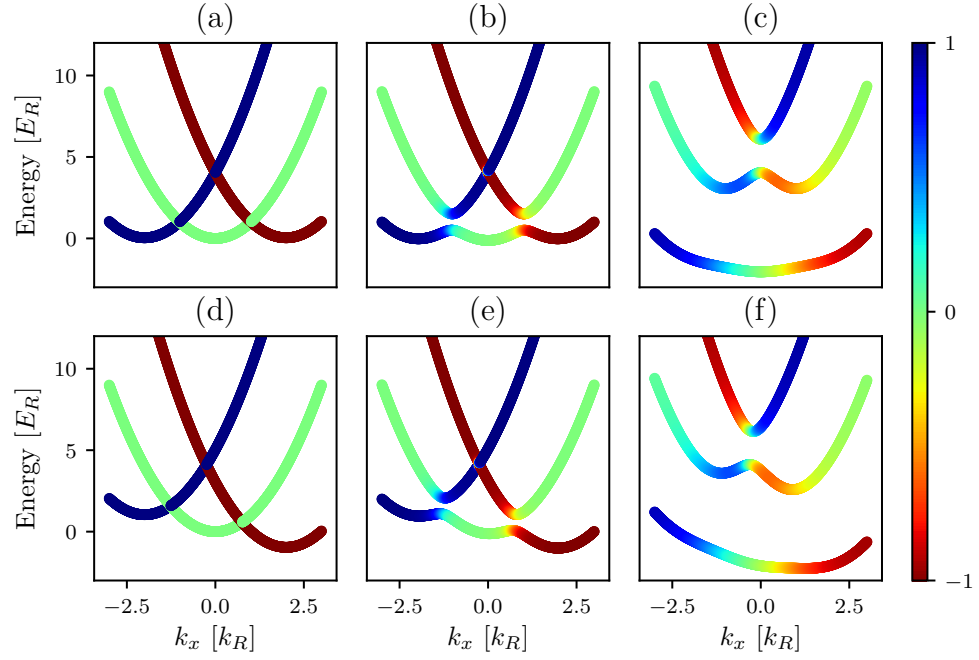
Figure 11: Band structure of the Raman Hamiltonian, Eq. **??**, in momentum space. For all plots, the quadratic Zeeman shift $\hbar\epsilon = 0.04 E_R$, and the color represents magnetization, labeled by the colorbar. (a) $\hbar\Omega = 0$, $\hbar\delta = 0$. (b) $\hbar\Omega = 1.0 E_R$, $\hbar\delta = 0$. (c) $\hbar\Omega = 5.0 E_R$, $\hbar\delta = 0.0$. (d) $\hbar\Omega = 0.0$, $\hbar\delta = 1.0 E_R$. (e) $\hbar\Omega = 1.0 E_R$, $\hbar\delta = 1.0 E_R$. (f) $\hbar\Omega = 5.0 E_R$, $\hbar\delta = 1.0 E_R$

coupled states. Then, during time-of-flight, apply a Stern-Gerlach gradient pulse to separate the spin compoenets and observe the fractional populations in different spin states as a function of Rabi oscillation time.

Figure **??**a,b shows example images obtained in time-of-flight when pulsing on an rf coupling field for atoms in the $F = 1$ and $F = 2$ manifold, respectively. The Stern-Gerlach gradient pulse separates the spin components along the horizontal axis in the images. The fractional population in each state can then be obtained by summing up the optical depth in each cloud and dividing by the total optical depth. Similarly, Figure **??**a shows an example time-of-flight image obtained when pulsing on a Raman coupling field on an $F = 1$ cloud initially in the $m_F = 0$ spin state. Here, the spin states are separated along the horizontal axis by the same Sternch-Gerlach pulse. In addition, the recoil momentum obtained when undergoing a Raman transition separates the different spin states along the vertical axis— parallel to the Raman beams along $\mathbf{e}_x$. The direction of the Stern-Gerlach gradient was chosen purposefully to be perpendicular to the Raman direction $\mathbf{e}_x$ for easy separation of the two effects.

These population oscillations can then be fit for coupling strength $\hbar\Omega$ and detuning $\hbar\delta$ Note that the quadratic Zeeman shift $\hbar\epsilon$ is set by the strength of the bias field B_0 and therefore often well known - we do not fit for this. The theoretic predictions are obtained by applying the time evolution operator $U = \exp(-iH_{\text{Raman/rf}}t/\hbar)$ to an initial state Ψ in the appropriate basis. Figure **??**c shows an example time series of rf pulsing in the $F = 1$ maifold, starting in the $m_F = 0$ state. The lines of best fit are overlayed on experimental data, extracting fit parameters $\hbar\Omega = 0.863 \pm 0.004E_R$ and $\hbar\delta = -0.198 \pm 0.007E_R$. Figure **??**d shows an example time series of rf pulsing in the $F = 2$ maifold, starting in the $m_F = -2$ state. Here, the extracted fit parameters were $\hbar\Omega = 1.000 \pm 0.002E_R$ and $\hbar\delta = -0.061 \pm 0.001E_R$.
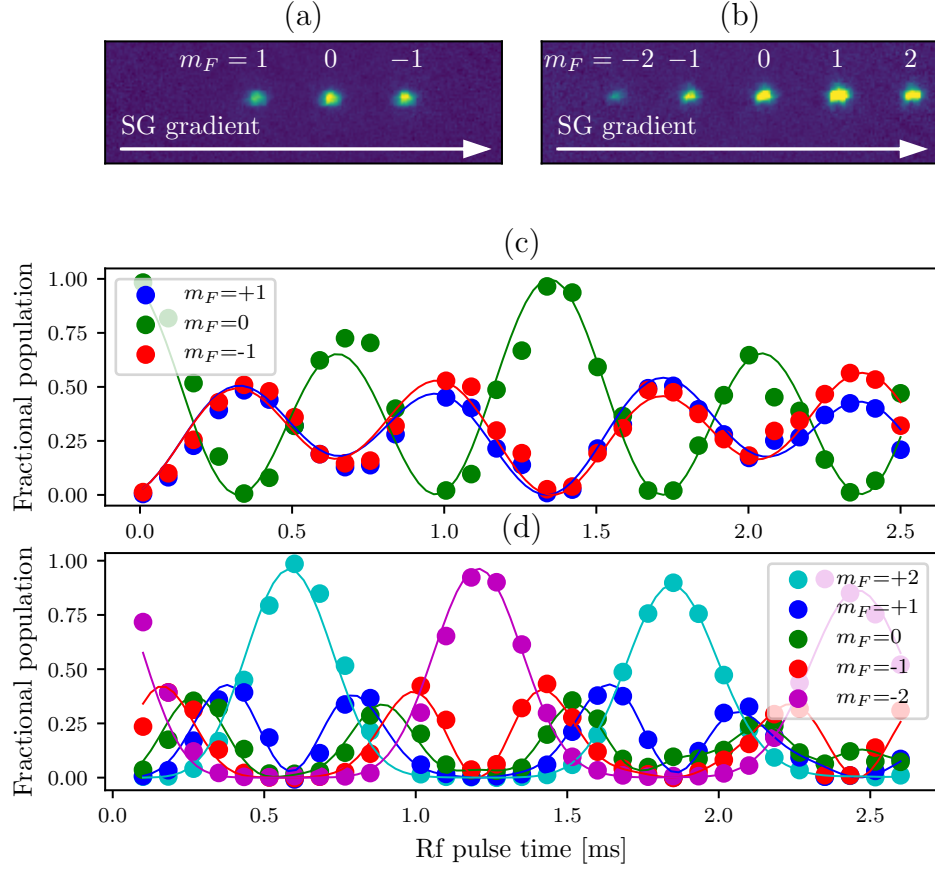
Figure 12: Pulsing on rf coupling. (a) Example time-of-flight image during an rf pusling experiment in the $F = 1$ manifold. Spin states are separated via a Stern-Gerlach pulse along the horizontal direction. (b) Example time-of-flight image during an rf pusling experiment in the $F = 2$ manifold. Here, 5 spin components are present. (c) Pulsing experiment in the $F = 1$ manifold. Dots represent fractional populations in different spin states measured from time-of-flight images, and lines repressent best fit theory curves. Fitted parameters are $\hbar\Omega = 0.863 \pm 0.004E_R$, $\hbar\delta = -0.198 \pm 0.007E_R$. (d)Pulsing experiment in the $F = 2$ manifold. Dots represent fractional populations in different spin states measured from time-of-flight images, and lines repressent best fit theory curves. Fitted parameters are $\hbar\Omega = 1.000 \pm 0.002E_R$, $\hbar\delta = -0.061 \pm 0.001E_R$. $\hbar\epsilon = 0.038E_R$ for all panels.
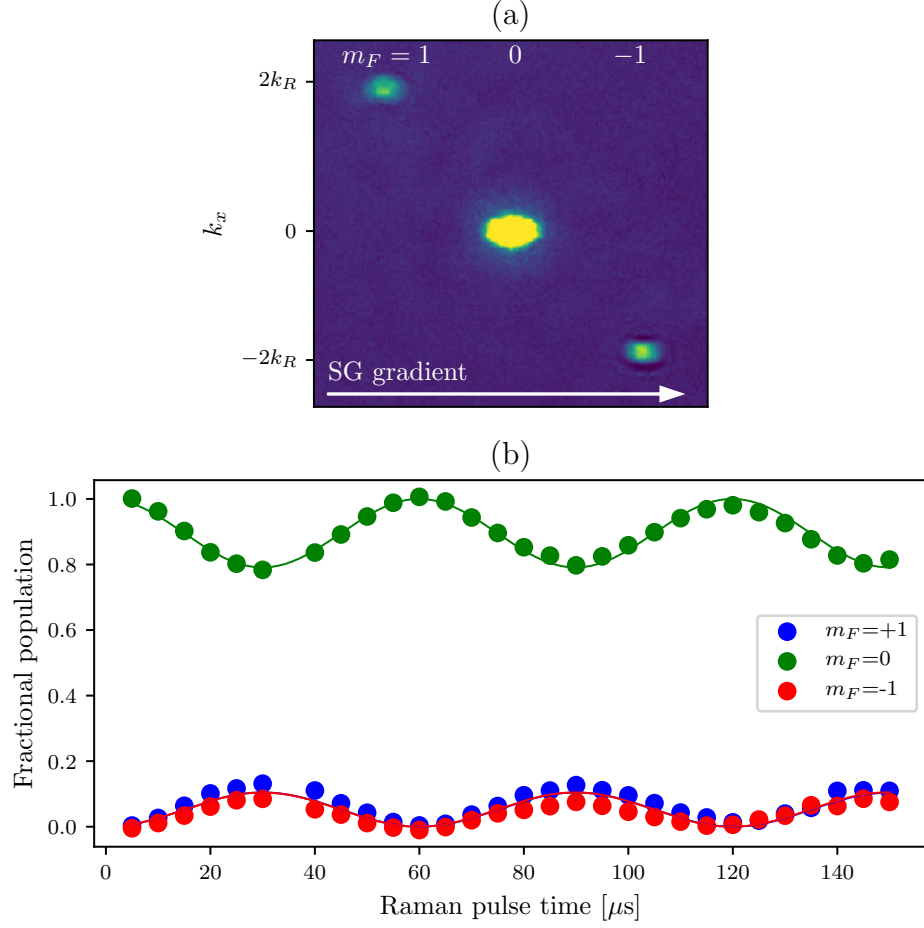
Figure 13: Pulsing on Raman coupling. (a) Example time-of-flight image during a Raman pulsing experiment in the $F = 1$ manifold. A Stern-Gerlach pulse during time-of-flight separates different spin components along the horizontal direction, and different momentum orders fly apart along the vertical direction. (b) Fractional population in different spin states during a Raman pulsing experiment as a function of time. Dots represent data and lines represent a best fit from theory. The fitted parameters are $\hbar\Omega = 1.47 \pm 0.01 E_R$, $\hbar\delta = 0.004 \pm 0.024 E_R$. The quadratic Zeeman shift was $\hbar\epsilon = 0.038 E_R$.

Figure **??**b shows an example time series of Raman pulsing in the $F = 1$ manifold, starting in the $m_F = 0$ state, with fitted parameters $\hbar\Omega = 1.47 \pm 0.01 E_R$ and $\hbar\delta = 0.004 \pm 0.024 E_R$. Note that although the coupling strength is almost double the rf coupling strenth in Figure **??**c, the contrast (peak to peak oscillation of the fractional population in, say, the $mF = 0$ state) is much lower in the Raman data than in the rf. This is a direct consequence of the recoil momentum transfer, and can be understood by looking at the band structure. For rf, the coupled bands at initial momentum $k_x = 0$ are separated by the coupling strength, see Figure **??**b. For Raman, even at zero coupling strength, due to the shifting of the parabolas by $2k_R$, and $k_x = 0$ the higher bands are $\hbar^2(2k_R)^2/2m = 4E_R$ separated from the lower bands. Therefore, the energy difference is larger and the fraction in the excited band will be lower, leading to lower contrast.

Bibliography

[1] Daniel Adam Steck. Rubidium 87 d line data. Available online, http://steck.us/alkalidata, April 2018. revision 2.1.5.

[2] T. G. Tiecke. Properties of potassium. Available online, http://www.tobiastiecke.nl/archive/PotassiumProperties.pdf, May 2011. v1.02.

[3] G. Breit and I. I. Rabi. Measurement of nuclear spin. *Phys. Rev.*, 38:2082–2083, Dec 1931.

[4] H.J. Metcalf and P. van der Straten. *Laser Cooling and Trapping*. Graduate Texts in Contemporary Physics. Springer New York, 1999.

[5] N.W. Ashcroft and N.D. Mermin. *Solid State Physics*. Saunders College, Philadelphia, 1976.

[6] Nicola Marzari, Arash A. Mostofi, Jonathan R. Yates, Ivo Souza, and David Vanderbilt. Maximally localized wannier functions: Theory and applications. *Rev. Mod. Phys.*, 84:1419–1475, Oct 2012.

[7] Karina Jimenez-Garcia. *Artificial Gauge Fields for Ultracold Neutral Atoms.* PhD thesis, Joint Quantum Institute, National Institute of Standards and Technology, and the University of Maryland, 2012.

[8] K. Jiménez-García, L. J. LeBlanc, R. A. Williams, M. C. Beeler, A. R. Perry, and I. B. Spielman. Peierls substitution in an engineered lattice potential. *Phys. Rev. Lett.*, 108:225303, May 2012.

[9] Daniel Adam Steck. Quantum and atom optics. Available online at http://steck.us/teaching, January 2015. revision 0.12.2.